JOURNAL OF AIRCRAFT
Vol. 34, No. 3, May–June 1997

# Experimental Results on a Mach 14 Waverider with Blunt Leading Edges

Michael Joseph Gillum*
*U.S. Naval Surface Warfare Center, Silver Spring, Maryland 20903-5640*
and
Mark J. Lewis†
*University of Maryland, College Park, Maryland 20742*

**The results of wind-tunnel tests of a Mach 14 waverider were analyzed to assess its overall performance. The waverider was optimized using a figure of merit that included viscosity, volume, and lift-to-drag considerations. The final design included a 0.25-in. leading-edge radius. The general performance of the tested waverider was analyzed and compared to the theoretical design from which it was derived. The theoretical design was generated from a conical flowfield, where the vehicle's infinitely sharp leading edges were everywhere-attached to the conical shock. Since the tested waverider featured blunt leading edges, it was important to assess the performance losses associated with flow spillage; these losses were found to be relatively small. However, the increased drag due to the blunt leading edges contributed greatly to reducing the aerodynamic performance of the tested waverider. Also, it was found that the aerodynamic coefficient data were insensitive to changes in Mach number and Reynolds number, indicating excellent off-design performance for the ranges of values tested.**

## Nomenclature

$B$ = bias error at 95% confidence level
$C_D$ = drag coefficient
$C_L$ = lift coefficient
$C_M$ = pitching-moment coefficient
$Cw$ = Chapman–Rubesin parameter, $(\rho u)_w/(\rho u)_\infty$
$L/D$ = lift-to-drag ratio
$M_\infty$ = freestream Mach number
$P$ = precision error at 95% confidence level, $t_{95}S$
$P_\infty$ = freestream pressure, psia
$Re$ = unit Reynolds number
$S$ = sample standard deviation
$t_{95}$ = 95th percentile point for Student's $t$ distribution
$U_{rss}$ = uncertainty $[B^2 + P^2]^{1/2}$
$XCP_p$ = pitch c.p., fraction of model length aft of nose
$\bar{\chi}$ = viscous interaction parameter

## Introduction

THE hypersonic waverider is a promising possibility for a high-performance hypersonic vehicle. Until recently, the design of waveriders served mainly as an academic exercise. Analytical waveriders having infinitely sharp leading edges and very slender bodies appeared to be impractical for realistic applications. With advancements in optimization theory, however, it has become possible to design waveriders with blunt leading edges, blunt noses, and respectable volumes that maintain high aerodynamic performance, thus making the waverider an attractive alternative to a conical or winged configuration.[1]

Prior to this test, even these optimized waverider designs were not readily accepted for practical applications. The analytical results predicting the optimized waverider's high performance have been successfully confirmed by computational fluid dynamics (CFD).[2–5] CFD, however, is often validated with comparable experimental or flight data, which for waveriders have been scarce.[3] Without flight or wind-tunnel testing, the waverider, albeit practically optimized, may remain overlooked for viable missions.

After more than two years of planning, a modified waverider design was tested in one of the U.S. Navy's most unique wind tunnels. At the Naval Surface Warfare Center (NSWC) Hypervelocity Wind Tunnel No. 9 in June 1993, McDonnell Douglas Aerospace and the U.S. Air Force Ballistic Missile Organization sponsored experimental tests of a realistically designed hypersonic waverider. Serving in an advisory capacity, the University of Maryland aided McDonnell Douglas Aerospace in the design of the Mach 14 waverider, optimized using a figure of merit that included viscosity, high volume, and high $L/D$. Furthermore, the final design included a 0.25-in. leading-edge radius. This radius was selected so as to represent the leading-edge heating requirements and to allow room for sufficient instrumentation to measure the heat transfer.

The analyses described here focused on two aspects of the wind-tunnel results for the Mach 14 waverider. First, the general performance of the waverider was analyzed and compared to the theoretical, infinitely sharp, leading-edge design from which it was derived. These results aided in assessing the performance losses associated with flow spillage from the lower surface to the upper surface because of leading-edge blunting. Second, the aerodynamic coefficients for the waverider were parameterized to facilitate quick calculations of these important performance parameters for use in trajectory simulations. Analytical estimates of the minimum drag coefficient were made and compared to the wind-tunnel data.

## Wind-Tunnel Test Background

### Aerodynamic Design

The aerodynamic design for the tested waverider was carried out by McDonnell Douglas using a modified version of the University of Maryland Axisymmetric Waverider Program (MAXWARP).[1,6] For the Tunnel 9 test, an infinitely sharp-

Presented as Paper 96-0812 at the AIAA 34th Aerospace Sciences Meeting, Reno, NV, Jan. 15–19, 1996; received May 23, 1996; revision received Feb. 10, 1997; accepted for publication Feb. 17, 1997.


*Aerospace Engineer, Dahlgren Division, White Oak Detachment, Re-entry Systems Branch. Student Member AIAA.
†Associate Professor, Department of Aerospace Engineering. Associate Fellow AIAA.

edged waverider was optimized on a figure of merit encompassing viscous *L/D*, and volume and wetted area. More specifically, an objective function was defined as follows:

$$\text{Objective Function} = \left(\frac{\text{Lift}}{\text{Drag}}\right)_{\text{Viscous}} \times \frac{(\text{Volume})^{2/3}}{\text{Area}_{\text{Planform}}} \quad (1)$$

This relationship provided a good compromise between the aerodynamic performance and the volumetric efficiency of the waverider. The design solution was driven toward the maximum of this objective function using a simplex method.[7] The design condition chosen was Mach 14 and $Re = 6.5 \times 10^6$ based on overall length.

The infinitely sharp-edged waverider was created with a sharp cone as the flowfield-generating body. The cone had a half-angle of 10.0 deg and, at Mach 14, generated a conical shock with a half-angle of approximately 11.66 deg. It was from within this conical flowfield that the sharp-edged waverider was carved out and its lower surface properties were defined. Specifically, the waverider's nosetip was displaced 70.0 in. from the vertex of the generating cone in the axial direction, and the waverider's spine (uppermost surface along centerline) was displaced 6.4 in. off the conical centerline. The lower surface properties were equivalent to those in the conical flow at every location, whereas the upper surface, assumed to be aligned with the freestream flow, had the same properties as the freestream. The sharp leading edge was everywhere-attached to the conical shock, thus preventing the higher pressure flow on the windward surface from spilling over the leading edge to the lower pressure leeward surface.

This infinitely sharp-edged waverider, representing the theoretical configuration, was then modified to include realistically blunted leading edges. To accommodate this feature, the upper and lower surfaces were separated at the sharp edges and were reconnected with 0.25-in. leading-edge radii. The resulting design had a length of 39.0 in., a span of 16.2 in., and a base height of 6.84 in. The waverider had a volume of 720 in.$^3$, with planform and base areas of 375 in.$^2$ and 64.6 in.$^2$, respectively. The planform area was used as the reference area for defining aerodynamic coefficients.

### Fabrication and Instrumentation

Using MAXWARP, a wire-frame geometry of the waverider was defined with a series of body coordinates at specified cross sections. These coordinates were transferred electronically from McDonnell Douglas to NSWC Tunnel 9 for fabrication of the wind-tunnel model.[8] The data were read into a solid-modeling computer aided design (CAD) system in which surfaces were fit to the frame and a solid model was created. Once the mechanical design was finalized, tool paths were generated for the parts and postprocessed for computer-numerically-controlled (CNC) machining. The details of this process are presented in Ref. 8.

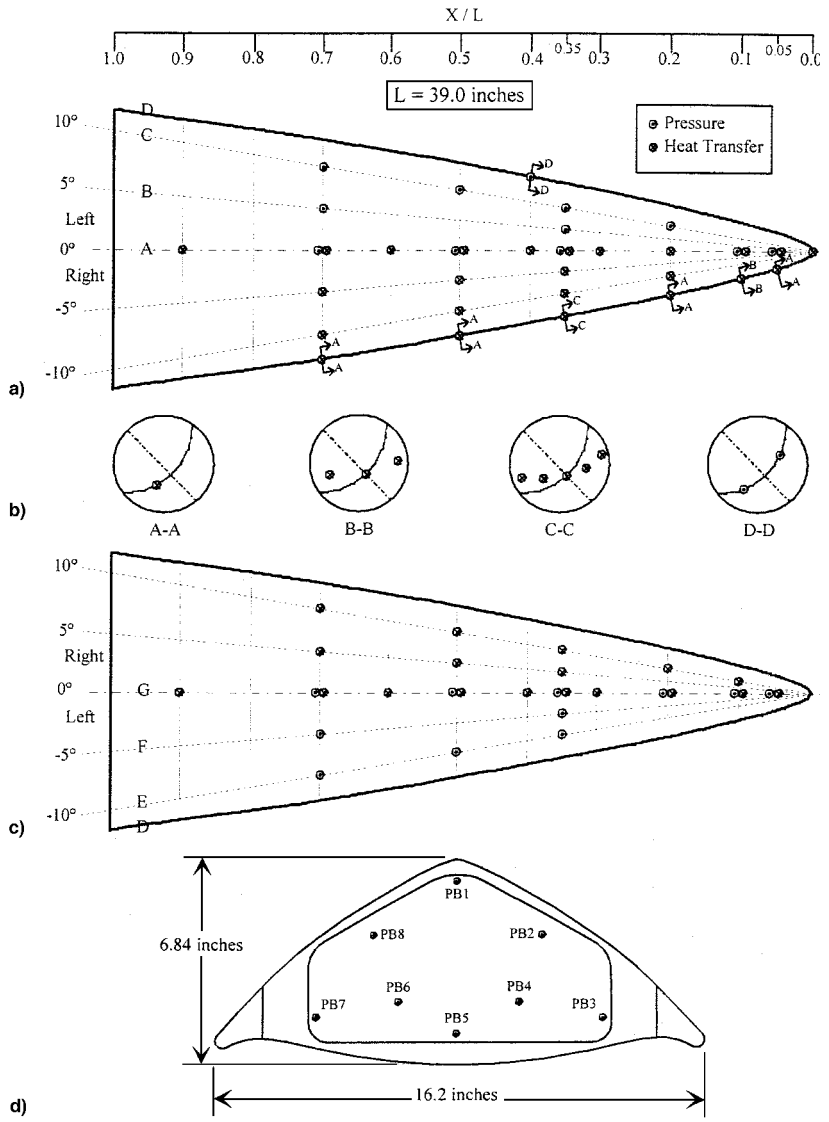


**Fig. 1 Wire-frame geometry of the waverider: a) top, b) leading-edge, c) bottom, and d) base views.**

The final wind-tunnel model was fabricated in eight parts. The nose, both leading edges, and the main instrumentation cavity cover plate were manufactured from 17-4 PH stainless steel. The remaining four sections were made from 6061-T6 aluminum.

The model was instrumented with a six-component force-and-moment balance, 32 pressure transducers (11 top, 11 bottom, 8 base, and 2 leading edge), and 48 coaxial thermocouples (17 top, 18 bottom, 1 nose, and 12 leading edge). The instrumentation was arranged along rays emanating from the model nose. Pressure transducers were confined to the left half of the model and coaxial thermocouples were confined to the right half. Figure 1 is a line drawing of the upper, lower, and base surfaces of the tested waverider, showing dimensions and the locations of the pressure and thermocouple instrumentation. Further details on the waverider instrumentation can be obtained from Ref. 9.

#### Test Facility

The NSWC Hypervelocity Wind Tunnel No. 9 is a blowdown facility that operates at Mach numbers of 7, 8, 10, 14, and 16.5. The testing of large-model configurations is made possible by a large test cell that is 5 ft in diameter and over 12 ft long. Tunnel 9 uses nitrogen as the working fluid. During a typical run a volume of nitrogen is heated and pressurized in a vertical heater vessel to the predetermined pressure and temperature required for the desired flow conditions. The test section and vacuum sphere are evacuated to a very low pressure, but remain separated from the heater by a pair of metal diaphragms. When the nitrogen in the heater reaches the proper conditions, the diaphragms are ruptured and the gas flows from the top of the heater and expands through the nozzle. As the hot gas exits the heater, cold gas from three pressurized driver vessels enters the heater base. This cold gas drives the hot gas in a piston-like fashion, thereby maintaining nearly constant conditions in the test cell during the run. Angle-of-attack sweeps up to 35 deg can be accomplished using a hydraulic pitch mechanism. More detailed information concerning the facility can be obtained from Ref. 10.

#### Test Matrix

A total of eight tunnel runs were accomplished in the test program. The test matrix was constructed to distinguish Mach number and Reynolds number dependence of the aerodynamic coefficients for the design, as well as to obtain some preliminary lateral stability information. Runs were first performed at the waverider's design point condition of Mach 14 and $Re = 2.0 \times 10^6$/ft. Two pitch–sweep runs and one yaw–sweep run were performed at this condition. Runs were also performed to investigate waverider off-design Mach number effects and Reynolds number effects, at Mach 10 and Mach 16.5, and $Re = 2.0 \times 10^7$/ft. Two runs were performed to investigate a temperature-sensitive paint, flow-visualization technique,[11] and to provide data to assess repeatability. Nominal run times were 0.2 s for a high Reynolds number run, 1.0 s for Mach 14, and 3.0 s for Mach 16.5. The identical pitch–sweep program was used for all runs except the high Reynolds number run. As a result, data were obtained over approximately 0.75 s for all runs.

#### Data Acquisition

For each run, the Tunnel 9 data acquisition and recording equipment (DARE) VI was used to sample and record all tunnel conditions, force data, pressure data, and heat transfer data. DARE VI is a simultaneous-sample-and-hold, single-amplifier-per-channel system with 14-bit resolution. The output signals of all the instrumentation were amplified and fed through six-pole low-pass Bessel filters with a cutoff frequency of 25 Hz before being recorded. The analog filters removed most 60-Hz electrical noise. The sample rate was 250 Hz for all of the runs. Complete descriptions of this process are given in Refs. 9 and 12.

#### Measurement Uncertainty

Measurement uncertainties were estimated using the principles set forth in Refs. 13 and 14. The specific procedures employed in Tunnel 9 are given in Ref. 15. In general, the uncertainty in a measurement was composed of a combination of fixed error or bias $B$, and random error or precision $P$. The rss model was used to estimate the uncertainties at the 95% confidence level:

$$U_{\text{rss}} = \pm[B^2 + P^2]^{1/2} = \pm[B^2 + (t_{95}S)^2]^{1/2} \quad (2)$$

For sample sizes greater than 30, $t_{95}$ is considered equal to 2. Bias and precision errors were propagated through to calculated results individually, then combined into overall uncertainties. Traceability of working standards to the National Institute of Standards and Technology was established through the Navy Metrology and Calibration Program and through manufacturer supplied calibrations. A more complete discussion of the measurement uncertainty for this test can be obtained from Refs. 15 and 16.

## Performance Comparisons with Theoretical Configuration

The measured performance of this tested waverider was compared to the predicted performance of the sharp-edged version from which it was derived. It was expected that crossflow would occur from the windward surface over the blunt leading edge to the low-pressure leeward surface, thus reducing the lifting capability as compared to the sharp-edged waverider. Furthermore, the addition of the blunt nose and leading edges increased the overall drag on the vehicle. Therefore, it would not have been surprising if the aerodynamic performance of the tested waverider was much poorer than that of the theoretical, sharp-edged design. Analytical discussions of such effects of leading-edge blunting on the aerodynamic performance are found in Refs. 17–19. The current focus is to compare actual, experimental results on the tested waverider, with theoretical predictions for the conical-flow-generated, infinitely sharp geometry.

One way of assessing this performance degradation was to compare the surface pressure distributions over both vehicles. The calculated surface pressure distributions on the sharp-edged waverider were compared to the measured data for the design condition. The exact locations of the pressure taps were related to the corresponding locations on the sharp-edged waverider. The values of pressure on both bodies were nondimensionalized by the freestream pressure, and these ratios, $P/P_\infty$, were compared.

Figure 2 is a plot of upper surface $P/P_\infty$ vs axial distance along the centerline for the design point conditions (angle of attack of 0.0 deg, Mach number 14.0, and $Re = 2.0 \times 10^6$/ft). Comparisons were made between the tested waverider and the sharp-edged waverider. Since the sharp-edged waverider was designed to have the upper surface everywhere-aligned with the freestream, the $P/P_\infty$ on this is everywhere-equal to unity at zero angle of attack. Figure 2 shows that the deviations from this value for the tested waverider were greater near the nose region and gradually diminished farther aft. The deviations ranged from approximately 400% at 1.755 in. from the nose to approximately 25% at 27.495 in. from the nose. These results clearly demonstrated the effects of the blunted nose and leading edges. Since a detached shock existed ahead of the nose, the stagnation-point value of $P/P_\infty$ was approximately 250. Although the flow rapidly expands around the blunted nose, the higher-pressure nose region influenced the pressure distribution several inches downstream. Simultaneously, flow

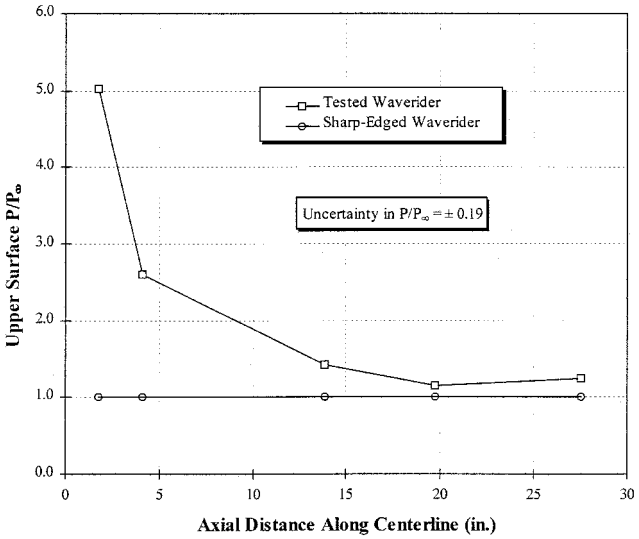


**Fig. 2 Comparison of axial variations in upper surface $P/P_\infty$.**

was spilling over the leading edges from the higher pressure lower surface and raising the pressures everywhere on the upper surface. Near the aft region, where the waverider was much wider, these leading edge effects became less pronounced near the centerline; however, they were not negligible.

Figure 3 is a plot of the lower surface $P/P_\infty$ variations along the centerline. Again, the large stagnation pressure caused large deviations in the nose region. However, the lower surface, being a windward surface, experienced an overexpansion similar to the behavior of a sphere–cone. A sphere–cone would experience a rapid expansion around the nose, an overexpansion downstream of the conical tangency point, and a gradual compression approaching the conical limit far downstream. The tested waverider exhibited similar characteristics here.

The predicted pressure distribution on the lower centerline of the sharp-edged waverider was relatively uniform, rising slightly toward the aft section. From waverider theory, the lower surface is defined along lines of constant stream function. This amounts to a locus of points residing on different rays within the conical flowfield. Along each conical ray the pressure is constant. The gradual changes in pressure for the sharp-edged waverider suggest that the waverider's lower surface was carved out of a region of relatively low-pressure gradients in the conical flowfield. This effect may also exist if the lower surface closely follows a single conical ray; however, this is not the case for this particular waverider. It can be shown that the slope at some lower surface points on this sharp-edged waverider is less than 10.0 deg. Since the generating cone had a half-angle of 10.0 deg, there are no conical rays within the flowfield making an angle less than this half-angle. Instead, this waverider lies far downstream, well away from the surface of the generating cone, and in a region of gradual pressure gradients.

Note that, at the last data point in Fig. 3, the measured pressure for the tested waverider was much higher than expected. This behavior was observed on each run at this gauge location whenever the gauge was inclined to the flow and does not reflect the expected behavior. This particular gauge differed from all other gauges, since it was one of only two flush-mounted gauges used on this model. These gauges were intended to measure high-frequency response in the boundary layer and were recorded on the high-speed data acquisition and reduction system. It is likely that the dynamics associated with this type of measurement caused this gauge to consistently overpredict the surface pressure whenever the gauge was windward.

Figure 4 is a plot of the upper and lower surface spanwise variations in $P/P_\infty$ for both the sharp-edged and tested waveriders at an axial location of 13.65 in. (35% of overall length). Since there were only three gauges on each side, it was difficult to determine exact trends; it was obvious, however, that the lower surface had lost pressure to the upper surface because of the spillover at the leading edge. The values of $P/P_\infty$ on the lower surface for the tested waverider were approximately 6% lower than the sharp-edged values, while the values on the upper surface were approximately 90% higher. Unfortunately, these numbers were not useful for determining the performance degradation experienced as a result of the blunt leading edges.

Although the details of the flowfields appeared to differ, the overall aerodynamic performance of the waverider was not greatly influenced. The maximum $L/D$ for the tested waverider was approximately 3.7. Theoretical results from MAXWARP predicted that the sharp-edged waverider would attain an $L/D_{max}$ of 4.61. This corresponds to a 20% degradation in $L/D$ because of vehicle bluntness. Since the tested waverider's leading edges were made overly blunt to exaggerate these effects, this is the largest degradation expected. It seems promising that a realistic waverider could be created with much sharper features and only suffer a degradation of a few percent.

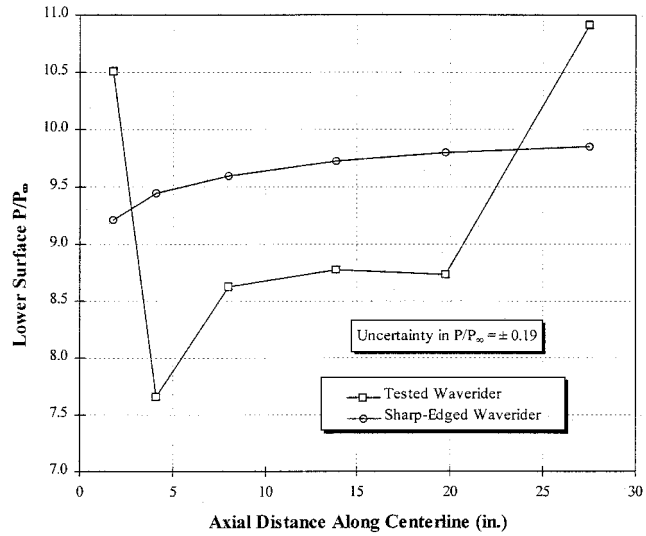


**Fig. 3 Comparison of axial variations in lower surface $P/P_\infty$.**

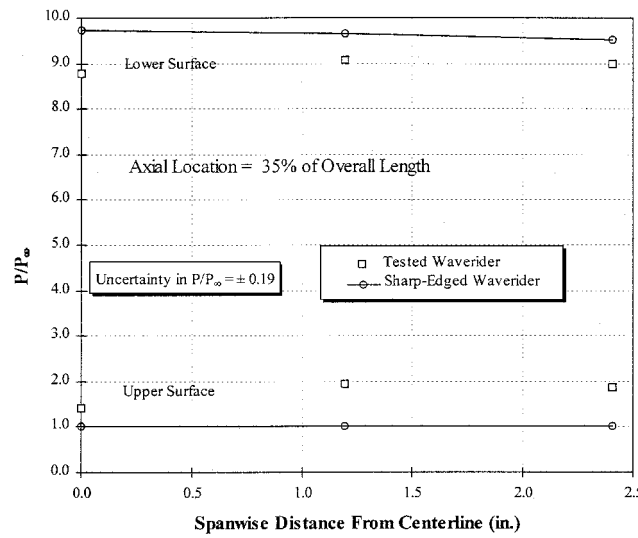


**Fig. 4 Comparison of spanwise variations in upper and lower surface $P/P_\infty$.**

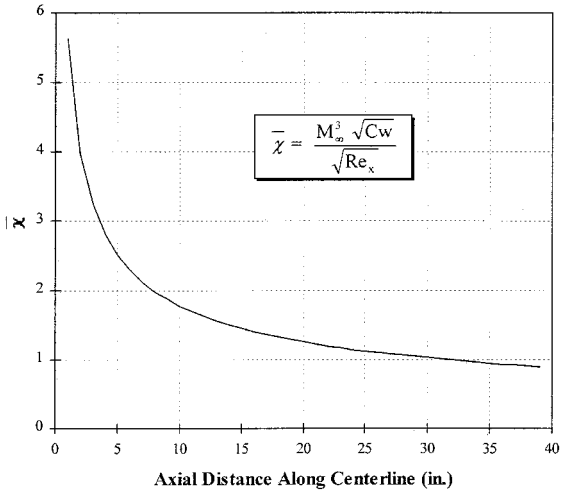


**Fig. 5 Axial variation in viscous interaction parameter for the tested waverider.**

Another contributor to the degradation in $L/D$ is viscous interaction. For the tested waverider, the axial variation in $\bar{\chi}$ is shown in Fig. 5, where

$$\bar{\chi} = M_\infty^3 \sqrt{Cw} / \sqrt{Re_x} \tag{3}$$

Values of $\bar{\chi}$ greater than three correspond to a strong viscous interaction. The presence of a strong viscous interaction, as evident in Fig. 5 near the nose of the tested waverider, results in a decrease in $L/D$. Furthermore, the strong viscous interaction near the nose causes an increase in surface pressure in that region. Since the viscous interaction effects increase the pressure and the skin friction, the overall drag on the vehicle will increase; furthermore, since this interaction is more pronounced on the upper surface, the increased pressure effect tends to decrease the lift. Therefore, the degradation in $L/D$ on a vehicle in the presence of strong viscous interactions may be substantial.

## Performance Parameterization

Since data were obtained over a large angle-of-attack range for the design condition of Mach 14, and since the coefficients appeared virtually insensitive to Mach number and Reynolds number changes, a parameterization of various aerodynamic coefficients may reflect these insensitivities and still accurately characterize the waverider's performance over a large range of flight conditions. Such parameterization would be of great value for trajectory calculations involving the waverider.

### Drag Coefficient

$C_D$ is often a desired quantity in a trajectory code; moreover, values of $C_D$ are usually required at every time step, amounting to as many as several thousand requests for $C_D$ at various flight conditions and configurations. The determination of $C_D$ using CFD would be computationally intensive, and so it is desirable to have a simple relation for the $C_D$ as a function of either $C_L$ or $\alpha$. Such a relation would provide quick feedback to a trajectory code.

The coefficient of drag is generally separated into a viscous term and an inviscid term as in Eq. (4):

$$C_D = C_{D_o} + KC_L^n \tag{4}$$

It can be shown that the exponent $n$ is equal to 3/2 for Newtonian flow. For tangent-wedge flow at low Mach number, $n$ is equal to 2, assuming small wedge angles. For high Mach number, $n$ is equal to 1.5 for tangent-wedge flow, again assuming small wedge angles.

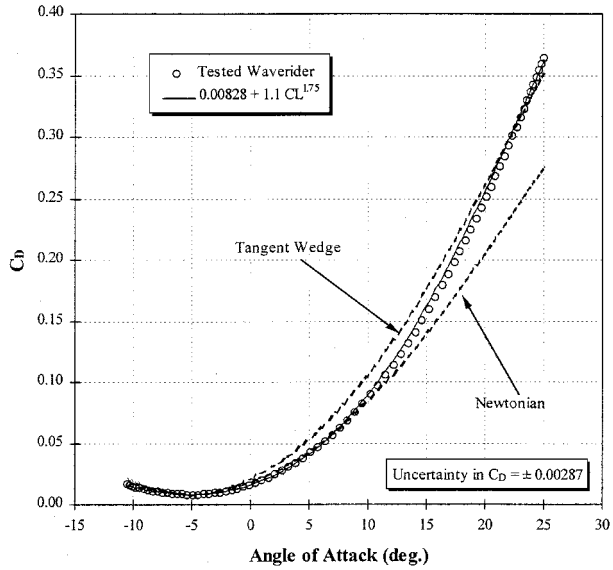


**Fig. 6 Parameterization of waverider drag coefficient.**

The values of $C_D$ for the waverider were parameterized against $C_L$ to obtain a best fit of the wind-tunnel data to Eq. (4). The resulting expression is given in Eq. (5):

$$C_D = 0.00828 + 1.1C_L^{1.75} (\pm 1.2\%) \tag{5}$$

Figure 6 shows the parameterized values of $C_D$ vs angle of attack compared to the actual wind-tunnel data. Also shown are the parameterizations using Newtonian flow and tangent-wedge flow. It is interesting to note that the exponent that best fits the waverider data is exactly equal to the average of the Newtonian and tangent-wedge values.

### Estimate of Minimum Drag Coefficient

Note that Eq. (5) contains a value of $C_{D_o} = 0.00828$. This corresponds to the value of the drag coefficient at which $C_L = 0$, or the minimum drag value as obtained from the test data. The minimum drag point occurred at an angle of attack of $-5.0$ deg. It is interesting to dissect this value and try to analytically predict this result. It will be assumed that this value includes skin friction drag, leading-edge drag, pressure drag, and base drag. Values for these components of $C_{D_o}$ will be estimated.

The laminar and turbulent shear can be estimated using the hypersonic correction to Reynolds analogy using the methods described in Ref. 20. These expressions, developed further in Ref. 21, using the details of the tested waverider, were used to calculate the laminar and turbulent skin friction drag on the upper and lower surfaces of the waverider for several angles of attack about the minimum drag point.

Accounting for the drag created by both blunt leading edges, Eq. (6) is a Newtonian approximation for the coefficient of drag on two blunt semicircular regions of constant radius of curvature, extending along a swept leading edge:

$$C_{D_{LE}} = \frac{2.4571 \cos^3 \phi R_{LE}}{A_{ref}} \int_{LE} \sin^3\theta \, ds \tag{6}$$

This equation[21] approximates each segment of the leading edge as a half cylinder of radius $R_{LE}$ oriented directly at an angle $\theta$ in the horizontal plane and constant angle $\phi$ in the vertical plane to the incoming flow. $S$ is the coordinate along the leading edge. For the waverider, the leading-edge radius $R_{LE}$ was 0.25 in., $\phi$ was 5.0 deg at the minimum drag angle of attack, the reference area (planform) was 375.3 in.$^2$, and the integral of the $\sin^3(\theta)$ with respect to $ds$ was 1.165 in. Substi-

**Table 1 Variations in laminar, turbulent, and average $C_{D_o}$ with angle of attack**

| Angle of attack, deg | $C_{D_o}$, laminar | $C_{D_o}$, turbulent | $C_{D_o}$, average |
|---|---|---|---|
| −10.0 | 0.01456 | 0.02001 | 0.01729 |
| −7.5 | 0.00845 | 0.01380 | 0.01113 |
| **−5.0** | **0.00650** | **0.01185** | **0.00918** |
| −2.5 | 0.00871 | 0.01404 | 0.01338 |
| 0.0 | 0.01513 | 0.02041 | 0.01777 |

tuting these values into Eq. (6) gives the total drag coefficient, because of the blunted leading edges, for the waverider at the minimum drag angle of attack. Since the inclination angle $\phi$ can be related to the angle of attack, the leading-edge drag will vary with the cube of the cosine of the angle of attack. Therefore, the leading-edge drag can be estimated for various angles of attack, as was done with the skin friction drag.

The pressure drag was determined by resolving the components of the pressure force on the upper and lower surfaces into the direction of drag. The surface pressures on the inclined surfaces of the waverider were approximated by conical flow values of surface pressure on sharp cones. The half-cone angle was chosen to match the inclination angle of the surface of interest on the waverider. Again, the inclination angle was directly related to the angle of attack.

The base drag was determined from the pressure forces acting on the base of the waverider in the direction of drag, as a function of angle of attack. The base pressure on the tested waverider was found to be approximately 45% of freestream pressure and this value was used in the calculations.

Finally, the total laminar and turbulent values for $C_{D_o}$, including skin friction, leading edge, pressure, and base drag, are given in Table 1 as a function of angle of attack. Also included in Table 1 are the averages of the turbulent and laminar values.

It appears that the tested value of 0.00828 is close to the average of the laminar and turbulent predictions. This is not surprising since it was known from the temperature-sensitive paint technique[11] that the flow over the waverider transitioned from laminar to turbulent. This transition occurred around 25% of the overall length of the model aft of the nose.

Finally, although the individual components of $C_{D_o}$ could be written as functions of angle of attack [like $C_L$ in Eq. (5)], their values do not vary greatly with angle of attack. Moreover, since the objective of this analysis was to obtain a simple expression for the coefficient of drag of the tested waverider, and Eq. (5) does reasonably well, using the estimates of $C_{D_o}$ and the expression in Eq. (5) will provide quick and accurate estimates of the drag coefficient for the tested waverider.

### Lift Coefficient

It may be more useful to a trajectory code to have an expression for $C_D$ as a function of $\alpha$ instead of $C_L$. For the waverider over the angle-of-attack range tested, the $C_L$ can be expressed as function of $\alpha$ in degrees as in Eq. (7):

$$C_L = 0.0076415(\alpha + 5 \text{ deg})^{1.25}(\pm 0.5\%) \tag{7}$$

This expression is plotted in Fig. 7. Therefore, for a given value of $\alpha$, in degrees, the corresponding value of $C_L$ can be determined. Using this value of $C_L$, the corresponding value of $C_D$ can then be determined.

Having obtained parameterized expressions for $C_D$ and $C_L$, a drag polar can be plotted. As shown in Fig. 8, plotting the $C_L$ vs the $C_D$ for all eight runs, and including the parameterized expressions, excellent correspondence was observed.

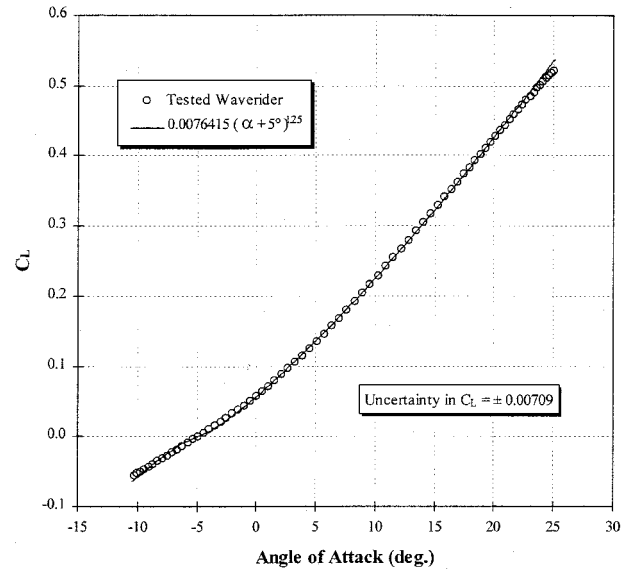


**Fig. 7 Parameterization of waverider lift coefficient.**

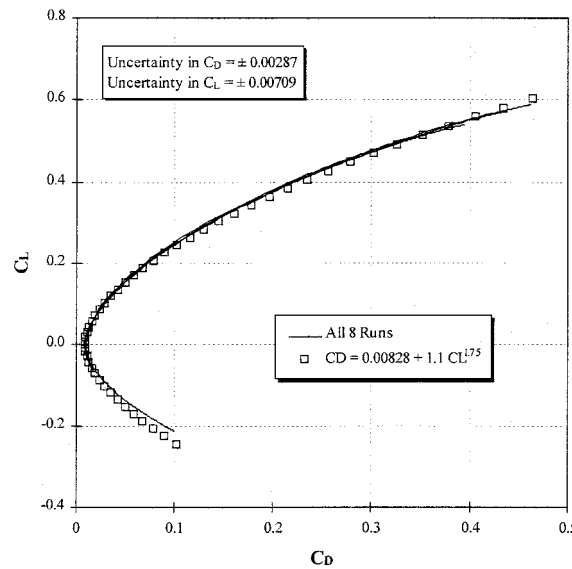


**Fig. 8 Parameterization of waverider drag polar.**

### Pitching Moment Coefficient

For the waverider over the angle-of-attack range tested, the $C_M$ can be expressed as function of $\alpha$ in degrees as in Eq. (8):

$$C_M = 0.0034(\alpha + 5 \text{ deg})^{1.4}(\pm 2.5\%) \tag{8}$$

This expression is plotted in Fig. 9. Therefore, for a given value of $\alpha$, in degrees, the corresponding value of $C_M$ can be determined.

Slight deviations around an angle of attack of −5 deg are the result of the $XCP_p$ becoming undefined as the moment coefficient is passing through zero; however, at larger angles of attack, Eq. (8) is within 1% of the measured values.

### $XCP_p$

The $XCP_p$ remained relatively constant during the run. The $XCP_p$ is undefined when the pitching moment coefficient passes through zero; consequently, large uncertainties exist at this point. The measured value of $XCP_p$ appeared to be slightly different on either side of this point. This point corresponds to an angle of attack of −5 deg. Therefore, one may define a

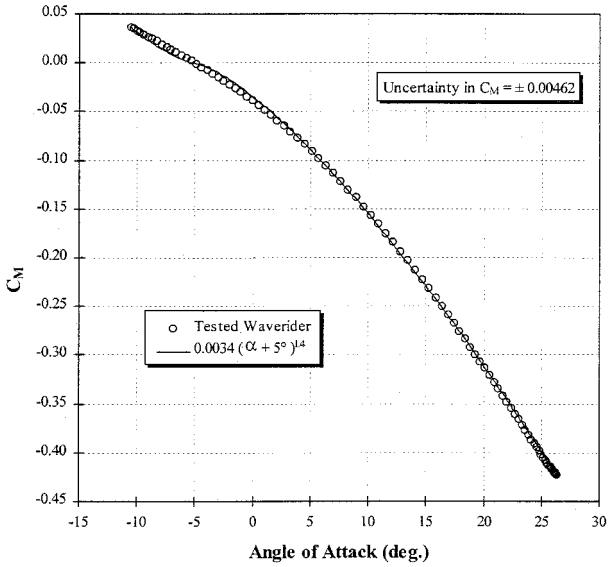


**Fig. 9 Parameterization of waverider pitching moment coefficient.**

value of $XCP_p$ as a fraction of the overall vehicle length, measured from the nose, for this waverider as follows:

$$XCP_p = 0.61 \qquad (\alpha < -7 \text{ deg}) \tag{9}$$

$$XCP_p = 0.64 \qquad (\alpha > -3 \text{ deg}) \tag{10}$$

**Yaw Data**

One run was performed to assess the yaw characteristics of the waverider. For this run, the vehicle was set at a constant angle of attack of 1.09 deg while swept through angles of yaw between −5 and +5 deg. This yaw-sweep range may appear small compared to the pitch-sweep range (−25 to +25 deg); however, this sweep should fully represent the expected angles of yaw that the waverider may experience in practice. In fact, it is unlikely that this hypersonic vehicle would be required to yaw more than ±3 deg for any given maneuver.

In general, the waverider performed quite well at these off-design conditions. The decrease in $L/D$ at the largest yaw angle was less than 5% of the unyawed value. Individually, the $C_L$ and $C_D$ decreased by less than 5 and 1%, respectively. The yaw moment coefficient appears to be extremely linear over the entire yaw sweep; moreover, the sign indicates that the tested waverider will be stable in yaw. This is an important result as it has been debated whether or not a waverider would become unstable when yawed. The data indicate that as the waverider is yawed, a restoring moment is developed that tends to return the vehicle to an unyawed attitude. A more thorough discussion of the yaw and off-design performance of the tested waverider can be found in Ref. 9.

## Conclusions

The present work examined the aerodynamic performance of a wind-tunnel-tested waverider that was designed and optimized to maximize $L/D$ and volumetric efficiency; furthermore, the waverider that was tested included blunted leading edges with 0.25-in. radii. Many of the observations indicate that the tested waverider may be a viable hypersonic flight vehicle worthy of serious consideration. It was found that the aerodynamic coefficients were insensitive to changes in Mach number and Reynolds number, indicating excellent off-design performance for the ranges of values tested.[12,16] The results also indicate that performance losses because of the blunted leading edges are not excessive, and could clearly be decreased by using less blunt leading edges.

Comparisons of the experimental data with predicted results were presented for the surface pressure on both the upper and lower surfaces. The predicted surface pressures were calculated from the generating vehicle's flowfield at the locations coincident to the tested waverider's surface. This effectively gives the surface pressure distributions over the theoretical or sharp-edged waverider. As expected, some of the higher pressure flow over the lower surface spilled over to the upper surface as a result of the blunted leading edge.

This effect was evident in pressures measured on the lower surface compared to those predicted to exist on the lower surface of the sharp-edged waverider. Likewise, higher pressures were measured on the upper surface than predicted to exist on the upper surface of the sharp-edged waverider. This effect, compounded by the increased drag because of the bluntness of the leading edges, is considered to be the primary reason for decreases in aerodynamic performance for the tested waverider, compared to the sharp-edged waverider. For instance, the maximum $L/D$ measured for the waverider was 3.7, whereas theoretical results of MAXWARP predicted an $L/D_{max}$ of 4.61. This degradation in $L/D$ is the result of flow spillage around the leading edges and the increased drag associated with the blunt nose and leading edges. Material selection and active cooling will permit the radius of the blunt edges to be reduced by as much as a factor of 10, resulting in less high-pressure flow spilling over to the leeward surface and, therefore, a greater $L/D$. Applying the Newtonian estimate for leading-edge drag to the MAXWARP prediction yields an $L/D_{max}$ of 4.07.

The aerodynamic performance of the waverider was parameterized to provide quick response for trajectory simulations. The coefficients of lift and drag, as well as the pitching moment coefficient and the axial c.p., were all parameterized. Estimates of $C_{D_o}$ were calculated for laminar and turbulent flow and included the effects of skin friction drag, leading-edge drag, pressure drag, and base drag. The resulting values seemed to bound the measured value, indicating that the flow over the tested waverider may have transitioned from laminar to turbulent. This agrees well with the results of the temperature-sensitive paint technique.[11]

## Acknowledgments

A portion of this work was performed under NASA Contract NAGW 3175 with Isaiah Blankson as Technical Monitor, to whom appreciation is expressed. Our sincerest appreciation goes to all those who made the wind-tunnel test possible. Many thanks to Dave Burnett of McDonnell Douglas Aerospace, the U.S. Air Force, and all those at the U.S. Naval Surface Warfare Center who maintain and operate Hypervelocity Wind Tunnel No. 9, especially Mark Kammeyer, who served as Project Engineer for this test.

## References

[1]Burnett, D., and Lewis, M., "A Re-Evaluation of the Waverider Design Process," AIAA Paper 93-0404, Jan. 1993.

[2]Takashima, N., and Lewis, M., "Navier Stokes Computation of Hypersonic Viscous Optimized Waveriders," *Journal of Spacecraft and Rockets*, Vol. 31, No. 3, 1994, pp. 383–391.

[3]Cockrell, C. E., Jr., "Interpretation of Waverider Performance Data Using Computational Fluid Dynamics," *Journal of Aircraft*, Vol. 31, No. 5, 1994, pp. 1095–1100.

[4]He, X., and Rasmussen, M. L., "Computational Analysis of Off-Design Waveriders," *Journal of Aircraft*, Vol. 31, No. 2, 1994, pp. 345–351.

[5]He, X., and Rasmussen, M. L., "Nonslender Waveriders," *Journal of Aircraft*, Vol. 31, No. 1, 1994, pp. 125–131.

[6]Vanmol, D. O., Lewis, M., and Anderson, J. D., Jr., "MAXWARP 2.0: Maryland Axisymmetric Waverider Program," Dept. of Aerospace Engineering, UMAERO 92-04, Univ. of Maryland, College Park, MD, 1992.

[7]Tincher, D. J., and Burnett, D., "A Hypersonic Waverider Flight Test Vehicle: The Next Logical Step," AIAA Paper 92-0308, Jan. 1992.

[8]Berry, C., Kammeyer, M., Larach, E., and Burnett, D., "Experiences in Fabrication of a Waverider Model for Wind Tunnel Testing," AIAA Paper 93-0510, Jan. 1993.

[9]Kammeyer, M. E., and Gillum, M. J., "Design Validation Tests on a Realistic Hypersonic Waverider at Mach 10, 14, and 16.5 in the Naval Surface Warfare Center Hypervelocity Wind Tunnel No. 9," U.S. Naval Surface Warfare Center, Dahlgren Div., TR-93/198, Silver Spring, MD, May 5, 1994.

[10]Ragsdale, W., and Boyd, C., *Hypervelocity Wind Tunnel 9 Facility Handbook*, 3rd ed., U.S. Naval Surface Warfare Center, Dahlgren Div., TR91-616, Silver Spring, MD, July 26, 1993.

[11]Liu, T., Campbell, B., and Sullivan, J. P., "Remote Surface Temperature and Heat Transfer Mapping for a Waverider Model at Mach 10 Using Fluorescent Paint," AIAA Paper 94-2484, June 1994.

[12]Gillum, M. J., Kammeyer, M. E., and Burnett, D., "Wind Tunnel Results for a Mach 14 Waverider," AIAA Paper 94-0384, Jan. 1994.

[13]"Measurement Uncertainty," *Performance Test Codes*, Vol. 19.1, American National Standards Inst./American Society of Mechanical Engineers, New York, 1985.

[14]Coleman, H., and Steele, G., *Experimentation and Uncertainty Analysis for Engineers*, Wiley, New York, 1989.

[15]Hedlund, E. R., and Kammeyer, M. E., "Aerodynamic and Aerothermal Instrumentation: Measurement Uncertainty in the NSWC Hypervelocity Wind Tunnel #9," AIAA Paper 96-2210, June 1996.

[16]Gillum, M. J., Kammeyer, M. E., and Burnett, D., "Details of a Mach 14 Waverider Wind Tunnel Test," AIAA Paper 94-2476, June 1994.

[17]Collinbourne, J. R., and Peckham, D. H. "The Lift and Drag Characteristics of Caret Wings at Mach Numbers Between 5 and 10," *Ministry of Technology, Aeronautical Research Council Current Papers*, 930, London, Feb. 1966.

[18]Squire, L. C., "Flow Regimes over Delta Wings at Supersonic and Hypersonic Speeds," *Aeronautical Quarterly*, Vol. 27, No. 1, 1976, pp. 1–14.

[19]Blosser, M. L., Blankson, I. M., Schwoerke, S., Brunson, D., and Hagseth, P., "Wing Leading-Edge Design Concepts for Airbreathing Hypersonic Waveriders," *Journal of Aircraft*, Vol. 32, No. 2, 1995, pp. 307–313.

[20]White, F. M., "Hypersonic Laminar Viscous Interactions on Inclined Flat Plates," *ARS Journal*, Vol. 32, No. 5, 1962, pp. 780, 781.

[21]Lewis, M. J., and Takashima, N., "Engine/Airframe Integration for Waverider Cruise Vehicles," AIAA Paper 93-0404, Jan. 1993.